Magnetic Resonance in Medicine 45:908–915 (2001)

Direct Reconstruction of Non-Cartesian *k*-Space Data Using a Nonuniform Fast Fourier Transform

Gordon E. Sarty,[1*] Raoqiong Bennett,[2] and Robert W. Cox[2]

An algorithm of Dutt and Rokhlin (SIAM J Sci Comput 1993;14: 1368–1383) for the computation of a fast Fourier transform (FFT) of nonuniformly-spaced data samples has been extended to two dimensions for application to MRI image reconstruction. The 2D nonuniform or generalized FFT (GFFT) was applied to the reconstruction of simulated MRI data collected on radially oriented sinusoidal excursions in *k*-space (ROSE) and spiral *k*-space trajectories. The GFFT was compared to conventional Kaiser-Bessel kernel convolution regridding reconstruction in terms of image reconstruction quality and speed of computation. Images reconstructed with the GFFT were similar in quality to the Kaiser-Bessel kernel reconstructions for 256^2 pixel image reconstructions, and were more accurate for smaller 64^2 pixel image reconstructions. Close inspection of the GFFT reveals it to be equivalent to a convolution regridding method with a Gaussian kernel. The Gaussian kernel had been dismissed in earlier literature as nonoptimal compared to the Kaiser-Bessel kernel, but a theorem for the GFFT, bounding the approximation error, and the results of the numerical experiments presented here show that this dismissal was based on a nonoptimal selection of Gaussian function. Magn Reson Med 45:908–915, 2001. © 2001 Wiley-Liss, Inc.

Key words: *k*-space; Fourier transform; reconstruction; ROSE scan; spiral scan

From a mathematical point of view, the most straightforward approach for the reconstruction of MRI data acquired on non-Cartesian trajectories in *k*-space, such as spiral (1–3), rosette (4,5) or ROSE (6) is to reconstruct directly via a Fourier summation (7,8). However, the computational complexity of the direct approach is usually an order of magnitude, or more, greater than an approach that uses the efficient fast Fourier transform (FFT) (9,10). Since the FFT requires that data be sampled on a uniform Cartesian grid in *k*-space, a popular method for the reconstruction of non-Cartesian sampled MRI data has been to regrid the data onto a Cartesian grid via a convolution regridding approach.

Jackson et al. (11) have argued that the Kaiser-Bessel function provides an optimal convolution kernel for convolution regridding reconstruction. In this work, we extend a method of Dutt and Rokhlin (12) for the computation of a generalized FFT (GFFT) for nonuniformly-spaced data to two dimensions. Given that Dutt and Rokhlin's approach is being considered for MRI reconstruction by other investigators (13), it is important to know the mathematical difference between the GFFT and convolution regridding. We show that the GFFT is equivalent to convolution regridding reconstruction with a Gaussian kernel, and that the new method provides a more accurate reconstruction in the same amount of time as the Kaiser-Bessel kernel-based reconstruction, especially for the smaller 64×64 pixel images that are frequently used for making functional MRI (fMRI) activation maps.

The work is organized as follows. In the Theory section, a quick review of Fourier transform image reconstruction is given, introducing the direct sum that needs to be efficiently computed. The method of Dutt and Rokhlin for computing 1D nonuniformly-spaced FFTs is reviewed next, followed by a description of the extension of the algorithm to two dimensions for MRI data reconstruction. In the Methods section, numerical experiments designed to compare the GFFT reconstruction to Kaiser-Bessel kernel convolution regridding reconstruction are described. The results of numerical experiments, including a rough timing of the algorithms, are described in the Results section. Finally, the meaning of the numerical experiments is covered in the Discussion section.

THEORY

The usual MRI signal model used for the development of Fourier transform image reconstruction algorithms is given by

$$S(t, \beta) = \int\int_{\mathcal{A}} \rho(x, y) e^{-2\pi i(xK_x(t,\beta)+yK_y(t,\beta))}\, dx\, dy \qquad [1]$$

where $\mathcal{A}$ is the region of the selected slice within the sensitive volume of the RF receiver coil, ρ represents the slice image of interest, and (x, y) is a point in that slice. The position $(K_x(t, \beta), K_y(t, \beta))$ of the data point $S(t, \beta)$ in *k*-space at a given point in time, t, and for a given acquisition interleaf, β, is proportional to the time integral of the applied magnetic gradient fields (14,15), $G_s(t, \beta)$, and $G_y(t, \beta)$, as given by

$$K_x(t, \beta) = \frac{\gamma}{2\pi} \int_0^t G_x(\tau, \beta)\, d\tau, \qquad [2]$$

$$K_y(t, \beta) = \frac{\gamma}{2\pi} \int_0^t G_y(\tau, \beta)\, d\tau$$

where γ is the gyromagnetic ratio.

[1]Department of Psychology, University of Saskatchewan, Saskatoon, Saskatchewan, Canada.

[2]Biophysics Research Institute, Medical College of Wisconsin, Milwaukee, Wisconsin.

Grant sponsor: NIH; Grant numbers: MH51358; NS34798; Grant sponsors: Medical Research Council of Canada; Health Services Utilization and Research Commission of Saskatchewan.

*Correspondence to: Gordon E. Sarty, Department of Psychology, University of Saskatchewan, 9 Campus Drive, Saskatoon, Saskatchewan S7N 5A5, Canada. E-mail: sarty@prana.usask.ca

Received 1 November 2000; accepted 1 December 2000.

If the k-space trajectory is nice enough (at least once continuously differentiable along the trajectory and continuously differentially interleavable, for example), the parameters t and β, which are naturally associated with the trajectory, can be used to form local coordinate systems on the k-plane called natural k-plane coordinate systems (8). In that case, the ideal, spatial frequency band-limited, image reconstruction is given by the positive operator, P_b, whose action is defined as

$$P_b\rho(x, y) = \int_{\beta_I}^{\beta_F} \int_{t_I}^{t_F} S(t, \beta) e^{2\pi i(xK_x(t,\beta)+yK_y(t,\beta))} |J(t, \beta)| \, dt \, d\beta \quad [3]$$

where $[\beta_I, \beta_F]$ and $[t_I, t_F]$ are the intervals on which β and t are defined, and $|J|$ is the absolute value of the determinant of the Jacobian of the transformation from the Cartesian k-plane coordinates to the natural k-plane coordinates. In practice, the MRI signal will be sampled at discrete points t_r, and β_s. A direct Fourier reconstruction (8) of the sampled data may then be obtained from a Riemann sum approximation of Eq. [3], ignoring the irrelevant constant $\Delta t \Delta \beta$, as given by the positive operator P whose action is given by

$$P\rho(x, y) = \sum_s \sum_r S(t_r, \beta_s) e^{2\pi i(xK_x(t_r,\beta_s)+yK_y(t_r,\beta_s))} |J(t_r, \beta_s)|. \quad [4]$$

More generally, if (t, β) do not define a natural k-plane coordinate system so that the Jacobian cannot be defined, the weighted correlation method (7) may be used to obtain a Riemann sum approximation of the integral

$$P_b\rho(x, y) = \iint_{\mathcal{B}} \hat{\rho}(k_x, k_y) e^{2\pi i(xk_x+yk_y)} \, dk_x \, dk_y \quad [5]$$

where $\mathcal{B}$ is a set containing the k-space data samples and $\hat{\rho}$ is the integral Fourier transform of ρ. Explicitly, the weighted correlation reconstruction is given by

$$P\rho(x, y) = \sum_s \sum_r S(t_r, \beta_s) e^{2\pi i(xK_x(t_r,\beta_s)+yK_y(t_r,\beta_s))} W(t_r, \beta_s) \quad [6]$$

where W is a weight that should minimize the difference between Eqs. [5] and [6]. A popular choice for W in that respect are the Voronoi areas associated with the k-space sample points (16). The Voronoi area associated with a k-space point is the area of the set whose points are closer to the given point than to all the other k-space sample points.

With conventionally acquired MRI data, the sample points $(K_x(t_r, \beta_s), K_y(t_r, \beta_s))$ lie on a Cartesian grid $(r\Delta k_x, s\Delta k_y)$ and $|J| = 1$ so that Eq. [4] reduces to

$$P\rho(x, y) = \sum_s \sum_r S(t_r, \beta_s) e^{2\pi i(xr\Delta k_x+ys\Delta k_y)}. \quad [7]$$

Typically, one will be interested in an $N \times N$ pixel image so that Eq. [7] needs to be computed N^2 times. Thus Eq. [7] will require $O((N^2)^2)$ multiplications and additions for the direct computation of $P\rho$ at N^2 points. By choosing $\Delta x = 1/(N\Delta k_x)$ and $\Delta y = 1/(N\Delta k_y)$, the FFT algorithm may be used to compute the N^2 values of the image at the points $(u\Delta x, v\Delta y)$, $u, v \in [-N/2, N/2]$, with $O(N^2 \log N)$ arithmetic operations. The direct computation of Eq. [7] requires on the order of hours of computational time for a typical 256^2 reconstruction, while the evaluation of Eq. [7] using the FFT is possible in a fraction of a second on modern computers. In the following section, a GFFT algorithm capable of computing the more general sum of Eq. [6] with $O((m(\epsilon)N \log m(\epsilon)N + m(\epsilon)N \log(1/\epsilon))^2$ arithmetic operations, where ϵ is the desired precision of the computation and m is an "oversampling" parameter, is described.

1D GGFT

At the heart of the GFFT is the need to compute

$$f_u = \sum_{k=0}^{M} \alpha_k e^{i\omega_k x_u} \quad [8]$$

for $u = 0, \ldots, N$, where $f_u \in C$, the set of complex numbers, $\alpha_k \in C$, $\omega_k \in [-N/2, N/2]$ and $x_u \in [-\pi, \pi]$, as a generalization of the well-known discrete Fourier transform (DFT) described by the equation

$$f_u = \sum_{k=0}^{N-1} \alpha_k e^{2\pi iuk/N} \quad [9]$$

for $u = 0, \ldots, N-1$. Using approximation theory, Dutt and Rokhlin (12) showed that the sequence $\{e^{i\omega_k x} | k = 0, \ldots, M\}$ can be approximated by the sequence

$$\left\{ e^{b(x/m)^2} \sum_{j=-q/2}^{q/2} P_{jk} e^{i(\mu_k+j)x/m} \,\middle|\, k = 0, \ldots, M \right\}$$

with precision ϵ, where m, b, and q are parameters chosen to meet the ϵ accuracy requirements, $\mu_k = [m\omega_k]$ is the closet integer to $m\omega_k$, and P_{jk} is defined by the formula

$$P_{jk} = \frac{1}{2\sqrt{b\pi}} e^{-(m\omega_k-(\mu_k+j))^2/4b} \quad [10]$$

for $k = 0, \ldots, M$ and $j = -q/2, \ldots, q/2$. Specifically, Dutt and Rokhlin's (12) Theorem 2.10 states:

Theorem 1 *Let $b > \frac{1}{2}$, $\omega_k \in R$, the set of real numbers, and let $m \geq 2$, $q \geq 4b\pi$ be integers. Let $\mu_k = [m\omega_k]$, then for any $x \in [-\pi, \pi]$,*

$$\left| e^{i\omega_k x} - e^{b(x/m)^2} \sum_{j=-q/2}^{q/2} P_{jk} e^{i(\mu_k+j)x/m} \right| < \epsilon(b, m)$$

$$= e^{-b\pi^2(1-1/m^2)}(4b + 9). \quad [11]$$

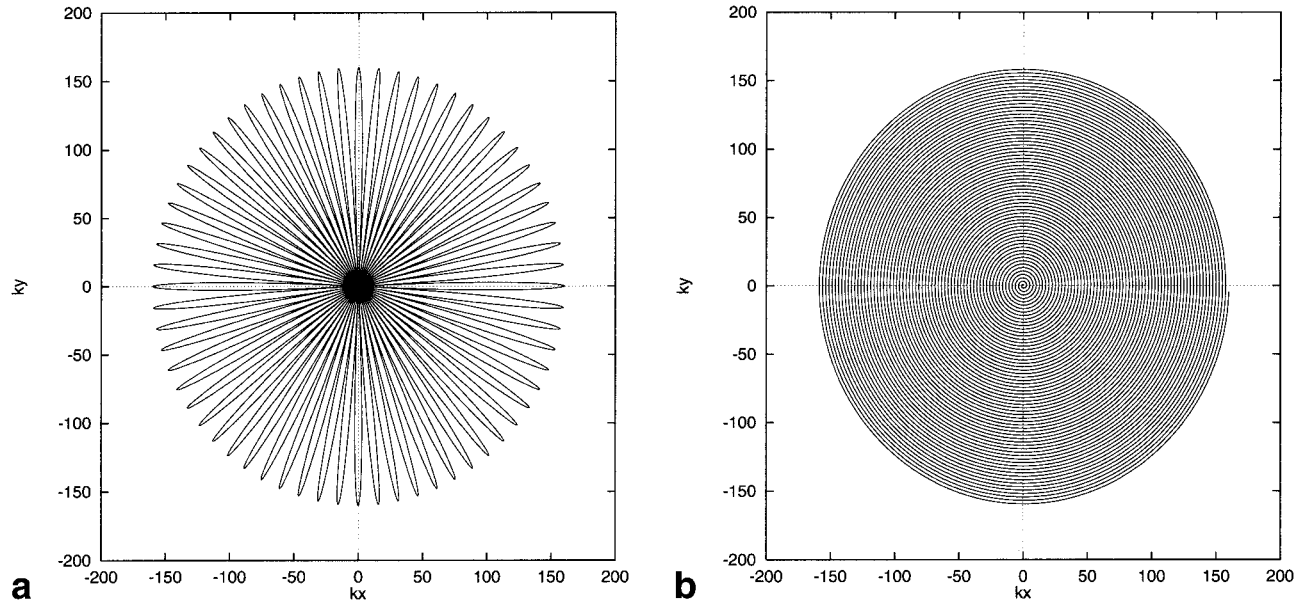

FIG. 1. *k*-Space trajectories used for the 64 × 64 image reconstructions: (**a**) ROSE and (**b**) spiral. The *k*-space radius A determines the resolution, and for our mathematical phantom's field of view of 0.2 m, the selection of A = 160 cycles/m for the 64 × 64 pixel and A = 640 cycles/m for the 256 × 256 pixel case was appropriate. For the 64 × 64 pixel case we set ω = 32 for the ROSE, ω = 64 for the spiral, and the number of samples for both to 8192. For the 256 × 256 pixel case we set ω = 128 for the ROSE, ω = 256 for the spiral, and the number of samples to 131,072 for both.

The substitution of $e^{b(x/m)^2} \sum_{j=-q/2}^{q/2} P_{jk}\, e^{i(\mu_k+j)x/m}$ for $e^{i\omega_k x_j}$ in Eq. [8] leads to a sum that may be computed with the help of the ordinary FFT in $O(mN \log mN + mNq)$ arithmetic operations. So Theorem 1 says that the DFT of a nonuniformly sampled set of N data points may be computed with an ordinary FFT of length mN with a precision that depends on the selection of m and the parameter b. While correct, Dutt and Rokhlin have shown through computational example that the error bound $\epsilon(b, m) = e^{-b\pi^2(1-1/m^2)}$ far overestimates the error obtained in practice, and the choice of $m = 2$ is sufficient for most practical applications. The selection of q affects the length, and hence the time required to compute, the sum in Eq. [11]. Therefore, the minimum value of q that gives an acceptable error is desirable. Since b is restricted in the hypothesis of the theorem to be greater than 0.5, the minimum value of q consistent with the hypothesis is $q = 8$ since the sum in Eq. [11] implies that q be an even integer.

2D GFFT

It will be convenient to re-index the *k*-space sample points from the two *r* and *s* indices, used in Eqs. [4] and [6] to a single index p so that $S(p) = S(t_r, \beta_s)$. Then we can write Eq. [6] as

$$P\rho(x, y) = \sum_{p=0}^{M} S(p)W(p)e^{i\omega_x(p)x}e^{i\omega_y(p)y} \qquad [12]$$

where $(\omega_x(p), \omega_y(p)) = 2\pi(K_x(t_r, \beta_s), K_y(t_r, \beta_s))$ and $W(p) = W(t_r, \beta_s)$. When natural *k*-space coordinates are defined, we may set $W(p) = |J(t_r, \beta_s)|$. In order to apply the GFFT as described below, it is necessary that $\omega_x(p)$, $\omega_y(p) \in [-N/2, N/2]$ and $x, y \in [-\pi, \pi]$. So, in practice it is necessary to scale the physical $K_x(p)$ and $K_y(p)$ coordinates to lie in the range $[-N/4\pi, N/4\pi]$. Let $\mu_p = [m\omega_x(p)]$, $\lambda_p = [m\omega_y(p)]$, $\alpha_p = S(p)W(p)$ and

$$\left.\begin{aligned} P_{jp} &= \frac{1}{2\sqrt{b\pi}}\, e^{-(m\omega_x(p)-(\mu_p+j))^2/4b} \\ Q_{jp} &= \frac{1}{2\sqrt{b\pi}}\, e^{-(m\omega_y(p)-(\lambda_p+j))^2/4b} \end{aligned}\right\} \quad \begin{aligned} j &= -\frac{q}{2}, \ldots, \frac{q}{2} \\ p &= 0, \ldots, M. \end{aligned}$$

Then, we may compute as good approximation to $P\rho$ of Eq. [12] the function $P_G\rho$ as given by

$$P_G\rho(x, y) = e^{b(x^2+y^2)/4} \sum_{p=0}^{M} \alpha_p \sum_{j_1=-q/2}^{q/2} \sum_{j_2=-q/2}^{q/2} P_{j_1p}Q_{j_2p}e^{i(\mu_p+j_1)x/2}e^{i(\lambda_p+j_2)y/2}. \qquad [13]$$

To compute the sums of Eq. [13] using the ordinary FFT, a discrete regular square grid of $N \times N$ image points $\{(x_u, y_v)\}$ is chosen, and the image reconstruction is computed as

$$P_G\rho(x_u, y_v) = e^{b(x_u^2+y_v^2)/4} \sum_{a=-mN/2}^{mN/2} \sum_{b=-mN/2}^{mN/2} e^{iax_u/2}e^{iby_v/2}\tau_{ab} \qquad [14]$$

where $x_u = 2\pi u/N$, $y_v = 2\pi v/N$, $u, v \in [-N/2, \ , N/2]$, and

Table 1
RMS and Maximum Absolute Differences With Direct Reconstructions and the Mathematical Phantom

	DT-PH	KB-PH	GFFT-PH	KB-DT	GFFT-DT
RMS (64^2 ROSE)	24.5	35.6	35.2	27.8	24.5
Max (64^2 ROSE)	132	232	212	204	186
RMS (64^2 spiral)	22.5	33.2	34.0	30.9	22.8
Max (64^2 spiral)	131	236	215	213	184
RMS (256^2 ROSE)	13.4	20.8	20.8	13.9	13.9
Max (256^2 ROSE)	138	248	248	221	221
RMS (256^2 spiral)	13.6	20.1	20.3	13.8	13.8
Max (256^2 spiral)	141	251	250	223	222

The column headings are: DT-PH, direct reconstruction minus original mathematical phantom; KB-PH, Kaiser-Bessel regridding reconstruction minus original mathematical phantom; GFFT-PH, GFFT reconstruction minus original mathematical phantom; KB-DT, Kaiser-Bessel regridding reconstruction minus direct reconstruction; GFFT-DT, GFFT reconstruction minus direct reconstruction. The GFFT reconstructions used $q = 10$, $b = 0.5993$.

$$\tau_{ab} = \sum_{\{p,j_1|\mu_p+j_1=a\}} \sum_{\{p,j_2|\lambda_p+j_2=b\}} \alpha_p P_{j_1 p} Q_{j_2 p}. \quad [15]$$

Eq. [14] may be computed using a $mN \times mN$ ordinary 2D FFT, which can be efficiently computed with $O(mN \log mN)^2$ arithmetic operations. The computation of each sum in Eq. [15] requires $O(mNq)$ arithmetic operations. Theorem 1 implies that $q \sim \log(1/\epsilon)$ so that $O(mN \log mN + mN \log(1/\epsilon))^2$ arithmetic operations are required to compute the GFFT. The use of the $mN \times mN$ FFT to compute the sums in Eq. [14] will give values of $P_G\rho(x_u, y_v)$ for u and v outside the interval $[-N/2, N/2]$. These extra values are discarded.

MATERIALS AND METHODS

Simulated MRI k-space data were generated on ROSE (Radially Oriented Sinusoidal Excursions) in k-space and spiral k-space trajectories (see Fig. 1) and reconstructed using the GFFT and convolution regridding with the following Kaiser-Bessel convolution kernel:

$$\psi(k_x, k_y) = \left[\frac{1}{L} I_0(\beta\sqrt{1-(2k_x/L)^2})\right] \times \left[\frac{1}{L} I_0(\beta\sqrt{1-(2k_y/L)^2})\right] \quad [16]$$

where I_0 is the zero-order modified Bessel function of the first kind. Jackson et al.'s (11) optimal values of $L = 4$ and $\beta = 12$ were used with regridding onto a 2 times "oversampled" grid. For each of the ROSE and spiral cases, two data sets were generated: one with high enough spatial frequencies suitable for the reconstruction of a 64×64 pixel image, and the other with high enough spatial frequencies suitable for the reconstruction of a 256×256 pixel image. For comparative purposes, the data were also reconstructed directly using Eq. [4]. In all reconstructions, the data were weighted with the natural k-plane coordinate Jacobian. The simulated signal was computed from the exact values of the integral Fourier transform of the Shepp and Logan (17) mathematical phantom following Eq. [1].

For the ROSE simulations, the following k-space trajectory was used:

$$(K_x(t), K_y(t)) = A\cos[2\pi\omega t](\cos[2\pi t + \beta], \sin[2\pi t + \beta]) \quad [17]$$

where $t \in [0, 1]$, A is the maximum k-space radius reached by the trajectory, and ω is a frequency. For both the 64×64 pixel and the 256×256 pixel cases, a single-shot trajectory ($\beta = 0$ only) was simulated. In practice, gradient slew-rate limitations will usually require interleaved acquisition for the 256×256 pixel case. However, other simulations have shown that the reconstruction of single-shot and interleaved ROSE (and spiral) data are very similar.

For the spiral simulations, the following simple Archimedean spiral k-space trajectory was used:

$$(K_x(t), K_y(t)) = At(\cos[2\pi\omega t + \beta], \sin[2\pi\omega t + \beta]) \quad [18]$$

where, again $t \in [0, 1]$. As with the ROSE simulations, only single-shot scenarios were simulated. Although spiral trajectories that make better use of available magnetic field

Table 2
RMS/Maximum Absolute Differences Between Various GFFT Reconstructions and the GFFT Reconstruction With $q = 10$, $b = 0.5993$ for the 64^2 Spiral Case

q	$b = 0.4$	$b = 0.5$	$b = 0.5993$	$b = 0.6$	$b = 0.7$	$b = 0.8$	$b = 0.9$
6	0.322/1	0.333/1	0.537/2	–	–	–	–
8	0.310/1	0.219/1	0.101/1	0.102/1	0.254/1	–	–
10	0.310/1	0.217/1	0/0	0.016/1	0.211/1	0.307/2	0.410/2

The blank entries indicate cases that were not simulated because they involve parameters well outside the hypothesis of Theorem 1. The underlined entries involve q and b that fall within the hypothesis of Theorem 1 (note that the $b = 0.5$ case is on the boundary of the hypothesis).

Table 3
RMS/Maximum Absolute Differences Between Various GFFT Reconstructions and the Kaiser-Bessel Kernel Regridding Reconstruction for the 64^2 Spiral Case

q	$b = 0.4$	$b = 0.5$	$b = 0.5993$	$b = 0.6$	$b = 0.7$	$b = 0.8$	$b = 0.9$
6	8.52/23	8.44/23	8.20/23	–	–	–	–
8	8.53/23	8.54/23	8.54/23	8.54/23	8.50/23	–	–
10	8.53/23	8.54/23	8.55/23	8.55/23	8.56/23	8.58/23	8.62/23

See footnote for Table 2.

gradient slew rates are known, the simple spiral serves to illustrate the properties of the various reconstruction methods.

Timing code was inserted into the reconstruction code to measure the CPU time required for each method. The time to compute the Jacobian weights was not measured, but since that computation is of $O(M)$ complexity, the time is not significant. Care was taken to avoid timing of code that included I/O. However, it should be noted that computation times varied by up to 20% depending on unavoidable system background processes. All reconstructions were done on a Sun Microsystems (Palo Alto, CA) Ultra5 computer with 256 MB of RAM running at a clock speed of 333 MHz. For comparison to array processors, it is noted that a 512^2 2D FFT, computed using the *Numerical Recipes in C* algorithm (18) required approximately 1.6 sec.

Theorem 1 restricts q to be larger than $4b\pi$ so that b is restricted to the interval $[0.5, q/4\pi]$ for the theorem to be valid. We also investigated cases where q and b were outside the limits covered by Theorem 1. For every GFFT case tested, root mean square (RMS) and maximum absolute differences between the GFFT reconstruction and the Kaiser-Bessel regridding reconstruction were computed, as were differences with the $q = 10$, $b = 0.5993$ GFFT reconstruction that Dutt and Rokhlin (12) have indicated is somewhat optimal. Differences between direct reconstructions, the "optimal" GFFT reconstructions, and Kaiser-Bessel regridding reconstructions were also computed since the intent of both the GFFT and Kaiser-Bessel regridding reconstruction is to approximate the sum of Eq. [4]. Finally, differences with the mathematical phantom were computed, but Gibbs ringing artifact at the phantom's edges made the differences difficult to interpret. All differences were reported in terms of grayscale values, which were between 0 (black) and 255 (white).

RESULTS

The Kaiser-Bessel kernel reconstructions required the following computation times: 15.0 and 14.1 s for the 256^2 ROSE and spiral images, respectively, and 1.05 and 0.74 s for the 64^2 ROSE and spiral images, respectively. The 256^2 ROSE and spiral GFFT reconstructions both required approximately 11.8 s for $q = 6$, 17.0 sec for $q = 8$, and 23.2 s for $q = 10$. The 64^2 ROSE and spiral GFFT reconstructions both required approximately 0.7 s for $q = 6$, 1.0 s for $q = 8$, and 1.4 s for $q = 10$. In comparison, the time required for direct reconstruction was very long. For the 64^2 ROSE and spiral reconstructions, 343 and 198 s of CPU time were required, respectively. The direct 256^2 ROSE and spiral reconstructions required overnight CPU time.

Gibbs ringing artifact around the bright phantom edges produces maximum reconstruction values that, if scaled so that the average value of the outer ring of the phantom was 255, would be greater than the original phantom maximum value. When the reconstructions were scaled to have a maximum value of 255 for display, as they necessarily would be in practice to avoid loss of reconstructed values, the overall grayscale values were depressed over the phantom values. As a result, differences between the reconstructions and the original phantoms tend to be large. Nevertheless, a smaller difference still implies a higher reconstruction accuracy. More precise mathematical comparisons of the reconstructions are possible, such as normalization based on the integral of the point spread function. However, the resulting correction would be difficult to introduce in practice, since the point spread function depends on many factors, and might result in the discarding of bright image values not due to Gibbs ringing. The RMS and maximum absolute differences between the Kaiser-Bessel kernel reconstructions, the GFFT reconstructions for $q = 10$, $b = 0.5993$, the direct reconstructions, and the phantom are given in Table 1.

The purpose of both the Kaiser-Bessel regridding method and the GFFT is to provide an approximate, but highly accurate, way to compute the sum of Eq. [4] efficiently. A measure of that accuracy may therefore be obtained by comparing the reconstructions to direct reconstructions. The RMS and maximum absolute differences between the two reconstruction methods and direct reconstruction are given in Table 1.

The remaining tables show differences between various GFFT reconstructions and the GFFT reconstruction with

Table 4
RMS/Maximum Absolute Differences Between Various GFFT Reconstructions and the GFFT Reconstruction With $q = 10$, $b = 0.5993$ for the 256^2 ROSE Case

q	$b = 0.4$	$b = 0.5$	$b = 0.5993$	$b = 0.6$	$b = 0.7$	$b = 0.8$	$b = 0.9$
6	0.148/2	0.198/2	0.332/2	–	–	–	–
8	0.415/1	0.101/1	0.066/1	0.067/1	0.161/1	–	–
10	0.145/1	0.102/1	0/0	0.010/1	0.111/1	0.161/1	0.206/1

See footnote for Table 2.

Table 5
RMS/Maximum Absolute Differences Between Various GFFT Reconstructions and the Kaiser-Bessel Kernel Regridding Reconstructions for the 256^2 ROSE Case

q	$b = 0.4$	$b = 0.5$	$b = 0.5993$	$b = 0.6$	$b = 0.7$	$b = 0.8$	$b = 0.9$
6	0.312/1	0.329/1	0.404/2	–	–	–	–
8	0.313/1	0.320/1	0.324/1	0.324/1	0.323/1	–	–
10	0.313/1	0.320/1	0.328/1	0.329/1	0.339/1	0.349/1	0.357/1

See footnote for Table 2.

$q = 10$, $b = 0.5993$, and between various GFFT reconstructions and the Kaiser-Bessel regridding reconstruction. Of the cases shown, the cases having $b = 0.4$ and $q = 6$ lie outside of the scope of Theorem 1. The cases $q = 8$, $b = 0.7$ and $q = 10$, $b = 0.8$, 0.9 also lie outside the scope of Theorem 1. Table 2 reports the RMS and maximum absolute differences between the various GFFT reconstructions and the GFFT reconstruction with $q = 10$, $b = 0.5993$ for the 64^2 spiral cases. Table 3 reports RMS and maximum absolute differences between the various GFFT reconstructions and the Kaiser-Bessel regridding reconstruction for the same 64^2 spiral cases. The results for the 64^2 ROSE cases were similar. Tables 4 and 5 report the differences for the 256^2 ROSE cases, with the results for the 256^2 spiral cases being similar.

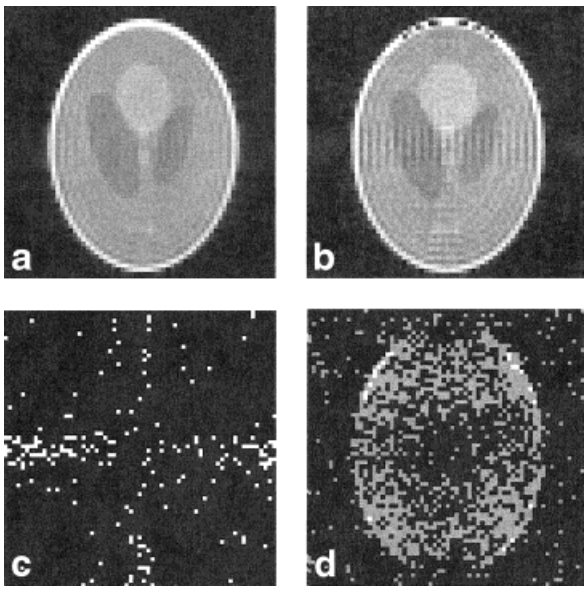

FIG. 2. **a:** A 64 × 64 reconstruction of the Shepp and Logan mathematical phantom using the GFFT with $q = 10$, $b = 0.5993$ and spiral k-space data. **b:** Absolute difference between the reconstruction in **a** and the Kaiser-Bessel regridding reconstruction. Differences between the Kaiser-Bessel reconstructions and other GFFT reconstructions that have q and b within the hypothesis of Theorem 1 are similar. **c:** Absolute difference between the reconstruction in **a** and the $q = 8$, $b = 0.5$ GFFT reconstruction. Differences of **a** with other GFFT reconstructions whose q and b parameters satisfy the hypothesis of Theorem 1 are similar. **d:** Absolute difference between the reconstruction in **a** and the $q = 6$, $b = 0.5993$ GFFT reconstruction. The large differences visible in **b** are due to different offsets of the maximum reconstruction value from the phantom value for the GFFT and Kaiser-Bessel regridding reconstruction. The offset difference is approximately 8 grayscale units (see Table 5). This large offset disappears for larger matrix reconstructions (see Fig. 3).

Figure 2, for the 64^2 spiral GFFT reconstruction, and Figure 3, for the 256^2 ROSE reconstruction, give some visual meaning to the numbers presented in the tables. The Kaiser-Bessel regridding reconstructions for both the ROSE and spiral 64^2 cases were approximately 23 grayscale units brighter than the GFFT reconstructions, a difference that could be detected visually. The difference in the two reconstructions was due to higher Gibbs ringing artifact in the GFFT reconstruction at the top of the phantom in the white border region. The higher reconstruction value in the bright outer ring, produced by Gibbs ringing, caused the rest of the image values to be scaled to a lower value since the reconstructions were scaled so that the highest reconstruction value was 255. The difference between the Kaiser-Bessel regridding and GFFT reconstructions for the 256^2 datasets were very small, especially when the GFFT reconstructions use q and b that are within the hypothesis of Theorem 1.

DISCUSSION

At first glance, Dutt and Rokhlin's algorithm appears elegant and unique. It certainly is elegant, with Theorem 1 giving an upper limit on the accuracy of the reconstructions. However, it is not unique. Close inspection of the method reveals that it is a convolution regridding method with the following Gaussian convolution kernel:

$$\psi(k_x, k_y) = e^{-(k_x^2 + k_y^2)/(2\sigma^2)} \qquad [19]$$

with $\sigma^2 = 2b/m^2$. The window width is q/m, and m is the amount of "oversampling." That is, an N^2 image is reconstructed through the FFT of an $(mN)^2$ Cartesian k-space dataset.

The use of the Gaussian regridding kernel has been studied by others. In particular, Jackson et al. (11) studied the $m = 2$ case with q between 3 and 10 and with b between 0.0898 and 0.2793. Since none of their parameters fall into cases covered by Theorem 1, it is not surprising that they concluded that a Gaussian kernel is not optimal. Jackson et al. used a Gaussian kernel that was too narrow to be optimal.

The Kaiser-Bessel method with $L = 4$ is almost identical to the GFFT method with $q = 8$, in terms of computational time. This is to be expected since sums of the form of Eq. [13] are the same length in each case. That is, the window width is 4 in both cases. The equivalent window widths for $q = 6$ and $q = 10$ are 3 and 5, respectively. Also, there

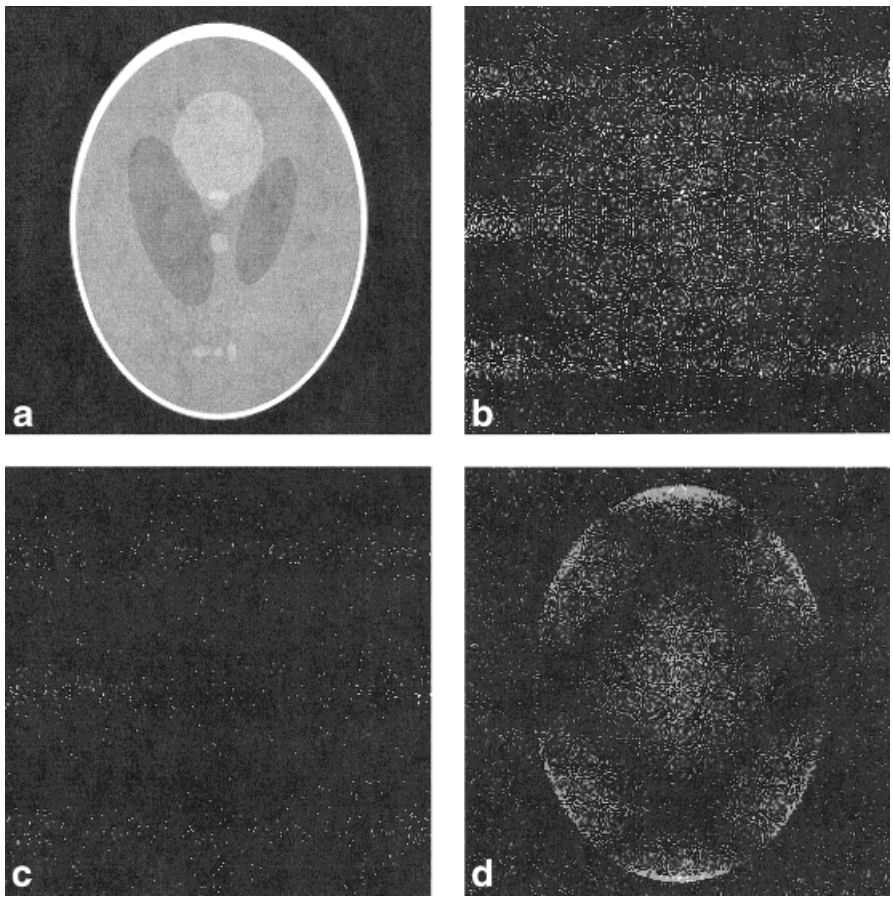

FIG. 3. **a:** A 256 × 256 reconstruction of the Shepp and Logan mathematical phantom using the GFFT with $q = 10$, $b = 0.5993$ and ROSE *k*-space data. **b:** Absolute difference between the reconstruction in **a** and the Kaiser-Bessel regridding reconstruction. Differences between the Kaiser-Bessel reconstructions and other GFFT reconstructions that have q and b within the hypothesis of Theorem 1 are similar. **c:** Absolute difference between the reconstruction in **a** and the $q = 8$, $b = 0.5$ GFFT reconstruction. Differences of **a** with other GFFT reconstructions whose q and b parameters satisfy the hypothesis of Theorem 1 are similar. **d:** Absolute difference between the reconstruction in **a** and the $q = 6$, $b = 0.5993$ GFFT reconstruction. The cause of the banding and cross patterns seen in the difference images is not known.

is very little difference in the complexity of the computer code, with the regridding code proper being roughly as complex as the code required to compute the sum of Eq. [15].

On the basis of the maximum difference between the phantom and the reconstructions (see Table 1), the GFFT appears to have a small edge over conventional Kaiser-Bessel regridding in terms of reconstruction accuracy, especially for the 64^2 pixel images. Note that the window for the GFFT reconstruction reported in Table 1 is 5, while the window for the Kaiser-Bessel kernel is 4, so it might be argued that the increased reconstruction accuracy of the GFFT reported in Table 1 is due to a larger window. However, the differences between the $q = 10$ (window width of 5) and $q = 8$ (window width of 4) cases reported in Table 2 are an order of magnitude or more smaller than the differences between the GFFT and the Kaiser-Bessel kernel reconstruction accuracy given in Table 1. Through Theorem 1, the GFFT is well understood mathematically, with explicit bounds on the errors involved in the approximation of Eq. [4]. The differences with the direct reconstructions reported in Table 1 suggest that the error of approximation of Eq. [4] is smaller for the GFFT than for the Kaiser-Bessel regridding method.

The results reported in Tables 4 and 5 and Fig. 3 show a very minor difference in the reconstructions obtained by either Kaiser-Bessel regridding or the GFFT for 256^2 pixel images whose pixel resolution is similar to the mathematical resolution as determined by the theoretical point spread function. The situation for the 64^2 pixel images is a little different (see Tables 2 and 3 and Fig. 2). In that case, the GFFT reconstructions have lower overall grayscale values as the result of Gibbs ringing caused by ripples in the point spread function. The Gibbs ringing offset error may be corrected in any reconstruction method by appropriately normalizing the reconstruction, but, as previously mentioned, such normalization may be difficult to implement in practice. In spite of the offset, the numbers in Table 1 indicate a higher reconstruction accuracy for the GFFT, especially in comparison to direct reconstruction. This indicates that the Kaiser-Bessel regridding method is trading reduced Gibbs ringing artifact, at least for the larger image values, for reduced reconstruction accuracy, possibly as a result of more smoothing in the reconstruction.

Comparisons of the GFFT reconstructions (Tables 2 and 4) show that there is very little variation in the reconstruction as long as the parameters q and b remain within the bounds implied by the hypothesis of Theorem 1. The errors begin to grow substantially when b falls outside the range $[0.5, q/4\pi]$ and q is less than $4b\pi$. The results of this study, and the independence of the error given by Theorem 1 on q above $4b\pi$, indicate that one should choose $q = 8$ to minimize the computational time and $b = 0.636$ $(=8/4\pi)$ to minimize the error, as predicted by Theorem 1. However, the results also indicate that the selection of $q = 6$ and $b = 0.4$, values which are outside

the hypothesis of Theorem 1, give accurate reconstruction with shorter computation time than Kaiser-Bessel regridding.

CONCLUSIONS

The nonuniform FFT of Dutt and Rokhlin (12) has been extended to two dimensions and applied to the task of reconstructing MRI *k*-space data collected on arbitrary trajectories in *k*-space. A close inspection of the method reveals it to be a standard convolution regridding method with a Gaussian kernel. Theorem 1 gives a quantitative bound on the error involved in the approximation of the direct reconstruction sum, and following the hypothesis of the theorem leads to an optimal selection of "gridding parameters."

The new reconstruction method, here called the GFFT, provides reconstructions that appear to be more accurate than the Kaiser-Bessel regridding method when similar regridding parameters are chosen. The computation time of the GFFT is similar to that of the Kaiser-Bessel regridding method, and may—as it may for the Kaiser-Bessel method—be reduced through the sacrifice of reconstruction accuracy. When combined with the results of Jackson et al. (11), the results obtained here indicate that regridding using the Kaiser-Bessel function with $\beta = 12$ and $L = 4$ or using the GFFT with $q = 8$ and $b \in [0.5, 0.636]$ provide equally optimal convolution regridding reconstruction in terms of convolution function selection. Jackson et al. (11) optimized their selection by minimizing aliasing energy. The optimal selection of the GFFT Gaussian convolution function here was made by minimizing the reconstruction error as quantified by Theorem 1.

When small, 64^2 image matrices are used, as is typical in functional MRI application, our results indicate that the Kaiser-Bessel kernel leads to smoother reconstructions with less Gibbs ringing artifact, while the GFFT Gaussian kernel leads to reconstructions that, overall, are more accurate.

ACKNOWLEDGMENTS

The technique assistance of Marco Pego is gratefully acknowledged. G.E. Sarty is supported by salary and operating grants from the Medical Research Council of Canada and the Health Services Utilization and Research Commission of Saskatchewan. R. Bennett and R.W. Cox acknowledge support from NIH grants MH51358 and NS34798.

REFERENCES

1. Ahn CB, Kim JH, Cho ZH. High-speed spiral-scan echo planar NMR imaging, vol I. IEEE Trans Med Imaging 1986;5:2–7.
2. Meyer CH, Hu BS, Nishimura DG, Macovski A. Fast spiral coronary imaging. Magn Reson Med 1992;28:202–213.
3. Noll DC. Methodologic considerations for spiral *k*-space functional MRI. Int J Imaging Syst Technol 1995;6:175–183.
4. Noll DC. Multi-shot rosette trajectories for spectrally selective MR imaging. IEEE Trans Med Imaging 1997;16:372–377.
5. Noll DC, Peltier SJ, Boada FE. Simultaneous multislice acquisition using rosette trajectories (SMART): a new imaging method for functional MRI. Magn Reson Med 1998;39:709–716.
6. Sarty GE. Critical sampling in ROSE scanning. Magn Reson Med 2000; 44:129–136.
7. Maeda A, Sano K, Yokoyama T. Reconstruction by weighted correlation for MRI with time-varying gradients. IEEE Trans Med Imaging 1988;7: 26–31.
8. Sarty GE. The natural *k*-plane coordinate reconstruction method for magnetic resonance imaging: mathematical foundations. Int J Imaging Syst Technol 1997;8:519–528.
9. Cooley JW, Tukey JW. An algorithm for the machine calculation of complex Fourier series. Math Comput 1965;19:297–301.
10. Brigham EO. The fast Fourier transform. Englewood Cliffs, NJ: Prentice-Hall; 1974.
11. Jackson JI, Meyer CH, Nishimura DG, Macovski A. Selection of a convolution function for Fourier inversion using gridding. IEEE Trans Med Imaging 1991;10:473–478.
12. Dutt A, Rokhlin V. Fast Fourier transforms for nonequispaced data. SIAM J Sci Comput 1993;14:1368–1383.
13. Kannengißer SAR, Brenner AR, Noll TG. Accelerated image reconstruction for sensitivity encoded imaging with arbitrary *k*-space trajectories. In: Proceedings of the 8th Annual Meeting of ISMRM, Denver, 2000. p 2967.
14. Twieg DB. The *k*-trajectory formulation of the NMR imaging process with applications in analysis and synthesis of imaging methods. Med Phys 1983;10:610–621.
15. Ljunggren S. A simple graphical representation of Fourier-based imaging methods. J Magn Reson 1983;54:338–343.
16. Rasche V, Proksa R, Sinkus R, Börnet P, Eggers H. Resampling of data between arbitrary grids using convolution interpolation. IEEE Trans Med Imaging 1999;18:385–392.
17. Shepp LA, Logan BF. The Fourier reconstruction of a head section. IEEE Trans Nucl Sci 1974;NS-21:21–43.
18. Press WH, Teukolsky SA, Vetterling WT, Flannery BP. Numerical Recipes in C. Cambridge: Cambridge University Press; 1992.